3D Microtomographic Study of Fluid Displacement in Rock Cores

M. Prodanović[a*], W.B. Lindquist[a*], and R.S. Seright[b†]

[a]Department of Applied Mathematics and Statistics, Stony Brook University, Stony Brook, NY 11794-3600, USA

[b]New Mexico Petroleum Recovery Research Center, New Mexico Institute of Mining and Technology, 801 Leroy Place, Socorro, NM 87801, USA

We report on three dimensional pore scale medium characterization and fluid displacement in a Berea (water wet) core. X-ray computed microtomography combined with X-ray attenuating dopants is used to obtain three dimensional images of two phase distributions at residual fluid conditions in the pore space. Employing numerical image processing algorithms based upon computational geometry to identify individual pores, throats, and fluid "blobs", we extract water and oil distributions at the level of individual pores in imbibition and drainage displacements.

We present results on the pore space characterization including distributions for pore volume, pore surface area, throat surface area, and principal direction diameters for pores and throats. We present results on oil and water distribution in the pore space at residual oil and water conditions. We also consider the effects on residual fluid distribution due to the injection and gelation of a water-based gel.

In extensive studies of Berea cores it has been observed that introducing water-based gels in the displacement process (for example, in water shut-off treatment of production wells) reduces permeability to water more than to oil. A number of micro-scale mechanisms [18] have been proposed for this disproportional permeability reduction. Our results provide supporting evidence for the involvement of gel dehydration and oil trapping while discounting gel blockage in throats as contributing mechanisms.

1. Introduction

Since the late 1980's, X-ray computed microtomographcy (XCMT) [6] has provided a tool for the non-destructive investigation of the three-dimensional microstructure of porous materials. We have been actively involved in developing numerical, image analysis tools to extract quantitative information on the stochastic nature of the microstructure of sandstones [8–12,20]. Since the late 1990's, the introduction of X-ray absorbant dopants to provide contrast between fluids has enabled nondestructive XCMT studies [18,19,22] of the three-dimensional distribution of fluids in the pores. This has the potential to

*Supported by US Department of Energy Geosciences Program, grant DE-FG02-92ER14261
†Supported by NPTO and NETL of the US Department of Energy, the State of New Mexico, ConocoPhillips, Intevep/PDVSA, Marathon, Shell, and the Ufa banch of YuganskNIPIneft

replace micromodel flow studies [14] where the network is dominated by two dimensional effects. We present improved results [18,19] on the partitioning of oil and water in Berea sandstone at residual fluid conditions. We also consider fluid re-partitioning effects and permeability changes due to the addition of an aqueous-based gel into the pore space.

The filling of pore space with an aqueous-based polymeric gel can reduce permeability to subsequent water flow by a factor of 10^4 [17] compared with single phase permeability to water in the absence of gel. Gel placement in two phase flow situations causes analagous, though disproportionate, phase permeability reductions. In particular we consider the residual resistance factor to oil, F_{rro}, defined as the ratio of relative permeability to oil flow at residual water conditions before and after gel placement, and the residual resistance factor to water, F_{rrw}, defined as the ratio of relative permeability to water flow at residual oil conditions before and after gel placement. In Berea cores, $F_{rro} \approx 10$ while $F_{rrw} \approx 10^3$. During field treatments when, for example, production wells are treated with gelants, some zones have high water saturation and high fractional water flow and other zones have high hydrocarbon saturation and fractional flow. After gel placement, in the oil zones, oil is the first fluid to flow through gel zones and F_{rro} and the mechanism determining its values are field-relevant. In water zones, water is the first fluid through gel zones and the permeability reduction factor of $\approx 10^4$ for water through aqueous gel is relevant. However, active management of fields, with the potential for long term, induced changes in flow patterns make the study of the disproportionate value for F_{rrw} also of scientific interest.

2. Experimental Procedure

A 6.5 mm diameter, 35 mm length core was prepared from a larger Berea sample having bulk absolute permeability 0.47 darcy and porosity of 22%. The core was saturated with brine containing 1% NaCl and 0.1% $CaCl_2$ and imaged at the tomographic facility on the X2B beam line [5] at the National Synchrotron Light Source at Brookhaven National Lab. Beam energy was 33.3 kev. A 2.52 mm long section centrally located along the length of the cylindrical core was imaged at 4.93 μm voxel resolution. Using the experimental setup described in [19], the core was successively imaged at residual fluid conditions occuring during a sequence of floodings. The experimental apparatus enabled the sequence of fluid injections to be performed without removing the core from the mounting stage.

The fluid injection sequence was: 35 pore volumes (PV) of oil; 70 PV of brine; 10 PV of aqueous gel; 20 PV of oil; 2.5 PV of brine. Fluid was injected with a pressure gradient of 17 psi across the length of the core. After gel injection, but before imaging, the core was heated to $\sim$ 60°C for 12 hours to effect gelation. The aqueous gel was Cr(III)-acetate-HPAM (hydrolyzed poly-acrylamide) consisting of (by weight) 0.5% Alcoflood 935 HPAM, 0.0417% Cr(III) acetate, 1% NaCl, and 0.1% $CaCl_2$. The oil was hexadecane doped with 10% (by weight) iodohexadecane. All experiments were performed at room temperature except during gelation. Fluid viscosities were: brine - 1 cp, hexadecane - 3.3 cp, gel - 20 cp.

Permeability measurements were recorded as a function of pore volumes injected during each injection sequence. Permeabilities used to compute F_{rro} and F_{rrw} were taken at the end of the sequence when residual conditions had been established. At the end of each injection stage, flow was halted (release of pressure gradient) while tomographic imaging

was performed. After each 3D image was acquired, the core was rotated to zero position to ensure not only that the same region was re-imaged after each flood but also to ensure voxel alignment between images.

From each image, a common $450 \times 450 \times 475$ μm (11.5 mm^3) rectangular region was subjected to image analysis. The size of the analyzed volume was determined by limitations of the 1 GByte of memory on the single processor hardware used for the image analysis. For purposes of reference, the sequence of images will be identified as s_w (brine saturated core), s_{wr} (residual brine after oil flood), s_{or} (residual oil after brine flood), gel (post gel injection), $gels_{wr}$ (residual brine post gel injection), and $gels_{or}$ (residual oil post gel injection).

3. Image Analysis

Using the software package 3DMA-rock [9,10,12], the images were analyzed for fluid distribution. The addition of iodohexadecane to the oil phase improves the X-ray attenuation contrast between the brine and oil phases, but at the cost of blurring the contrast between the oil and rock phases. Consequently the location of the rock phase is determined solely from the s_w image; rock location in subsequent images in the sequence is then inferred from its location in s_w. The geometry of the pore space is analyzed using the image s_w as described in [10]. In particular pore volume and throat area distributions are obtained. It is important to note that our division of the pore space is into pores separated by triangulated throat surfaces and is **not** a division into pores separated by channels. (We know of no geometrical measure to decide where a pore stops and a connecting channel begins in real rock void space.) Thus the **entire** volume of the pore space is divided into pores.

New to our analysis is the computation of pore surface area. As counting voxel faces [1] can lead to large errors in surface area computation, we utilize marching cubes [2,13] which provides a more reliable [4] triangulated surface from which to measure area. Pore surface areas are computed by "sealing" each throat opening with a (6-connected) set of voxels. This set consists of those voxels that are cut by the triangulated throat surface. The surface area of each pore is therefore the area of the triangulated interface, computed by the marching cubes algorithm, which separates the void space of the pore from the rock/throat voxels sealing that pore.

In images s_{wr} through $gels_{or}$, the rock matrix is identified from the analysis of s_w. The fluid filled space is then subjected to binary segmentation using a kriging based algorithm [15], to separately identify oil and brine phases (the water based gel is indistinguishable from brine phase). In addition to determining oil and brine saturations for the entire image, by inserting the throat surfaces determined in s_w into the pore space of the rest of the images, saturations can be determined on a pore-by-pore basis.

Each fluid phase is separately analyzed. We characterize the connectivity of each fluid phase by computing the number, location and size of the individual disconnected "blobs" of each phase. In computing connectivities of the two fluid phases, it is important to retain a 6-connected, 26-connected distinction between the two phases. We treat the wetting phase as 26-connected (the brine phase in the case of Berea) and the non-wetting phase (oil in Berea) as 6-connected. We are also interested in the "pore occupancy" of

each phase [3], where the pore occupancy of a blob is defined as the number of pores it spans.

4. Results

Fig. 1(a) shows a small region of a slice from the image stack acquired when the pore space was brine saturated. In addition to the visible pore space and sandstone grains, there appear highly attenuating impurities (e.g. feldspar) in the rock matrix, as well as the suggestion of some clay in the pore space. Effectively in our analysis, the clay filled regions are treated as grain. Fig. 1(b) shows the same region in the s_{or} (residual oil) image. Hexadecane occupancy in areas of the pore space is clearly visible. Fig. 1(c) is a composite picture showing the pore/rock segmentation resulting from Fig. 1(a) superimposed on the brine/hydrocarbon segmentation resulting from Fig. 1(b.)

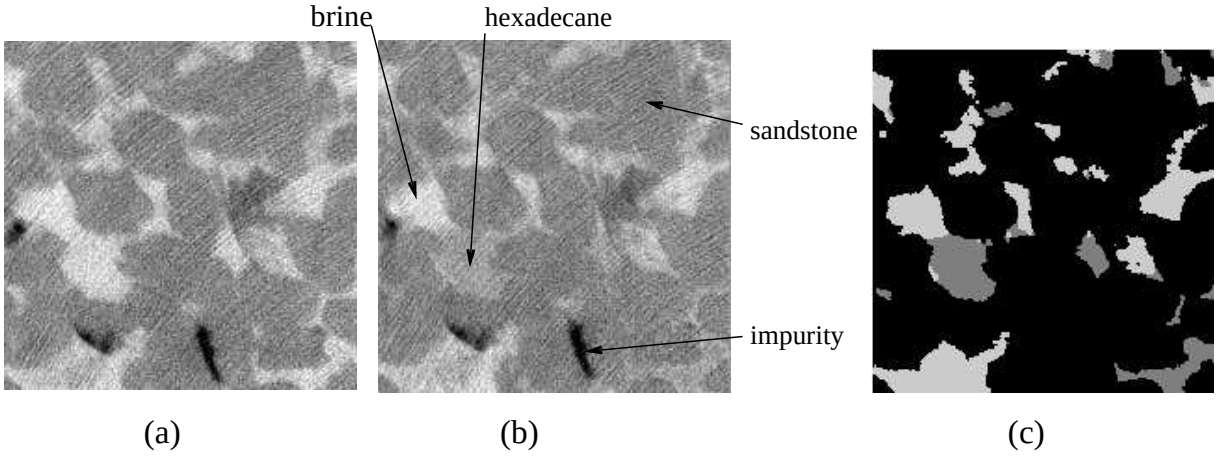

Figure 1. a) A subregion in s_w. b) The same region in s_{or}. c) Pore/rock and brine/oil segmentation results for this region.

Pore space characterization. Analysis of s_w gives a porosity of 18% for the imaged subregion of the Berea sample. The pore volume distribution determined from s_w is shown in Fig. 2. Paralleling the results of our analysis on Fontainebleau sandstone cores [10,11], the pore volume distribution is seen to be log-normal, with mean pore volume $2.6 \cdot 10^{-4}$ mm^3.

The center-of-mass location and the three principal directions were determined for each pore using a moment-of-inertia analysis. Three principal diameters were determined for each pore by measuring the pore width through the center of mass along each of the principal directions. The diameters are labeled D_1, D_2 and D_3 in decreasing length. In addition, an effective radius R_{eff} for each pore was determined from the sphere of equivalent volume. The distributions determined for $D_i, i = 1, 2, 3$ and R_{eff} are displayed in Fig. 2. Interestingly, the distribution of the smallest pore **diameter** D_3 and that for the equivalent sphere **radius** R_{eff} are strikingly similar. We have also computed the pore diameters along the $x-$, $y-$ and $z-$directions through the center of mass. These directions should be arbitrarily oriented with respect to the pore principal directions (assuming

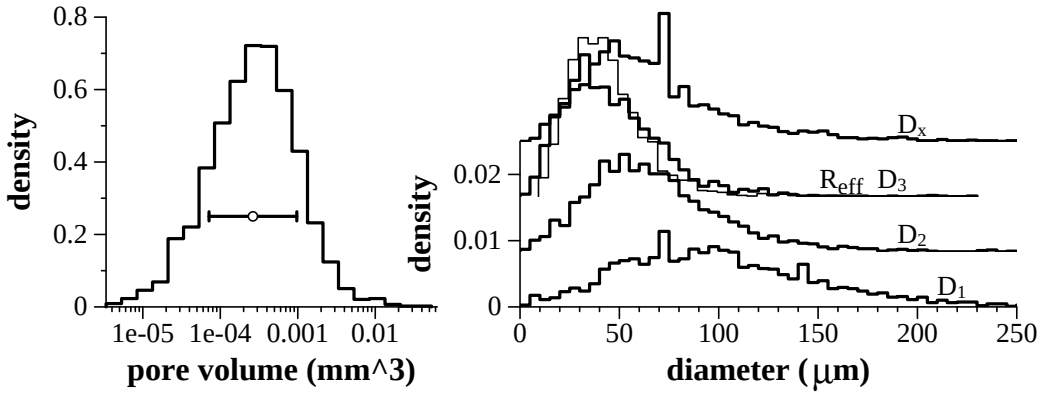

Figure 2. (left) Pore volume and (right) pore diameter distributions determined from s_w. (left) The open circle and horizontal bar indicate mean and standard deviation of the distribution. (right) All plots are to the same vertical scale, but D_1, D_2, D_3 and D_x, have been vertically displaced from each other for visual clarity. R_{eff} (light curve) is drawn with the same vertical displacement as D_3 to demonstrate the similarity between the two plots.

pore isotropy) and should produce distributions similar to each other and (given the pore anisotropy seen in $D_1 \rightarrow D_3$) different from the $D_1 \rightarrow D_3$ distributions. The distribution D_x for diameters measured in the x-direction is also displayed in Fig. 2. The D_y and D_z distributions are virtually identical to D_x, even to the elevated density occuring over the diameter range 70-75 μm. This elevated density corresponds to the peak in the D_1 distribution and presumably occurs whenever the largest principal axis direction of a pore aligns with one of the $x-$, $y-$ or $z-$ directions.

Pore and throat surface area distributions determined from s_w are shown in Fig. 3. The pore surface area distribution also appears to be log-normal, with mean value corresponding to a surface area of 0.043 mm^2. Note the surface area of a pore in this plot includes the surface area of its throats. As for pores, diameters along the two principal directions were determined for each throat surface, as well as an effective radius determined from the circle of equivalent area. The diameters are labeled D_1 and D_2 in decreasing length. The distributions determined for D_1, D_2 and R_{eff} are displayed in Fig. 3. Analogous to pores, the distribution of the smallest throat **diameter** D_2 and the equivalent circle **radius** R_{eff} are strikingly similar. The effect of voxel resolution is clearly seen as a sharp cut-off at the left side of both the throat surface area and diameter distributions.

Fluid characterization. Water saturations measured in the imaged region are compared in Table 1 with bulk determinations performed in independent experiments. Our determinations of s_w and s_o at s_{wr} and s_{or} are somewhat low, though agreement improves remarkably for gel and gels$_{or}$.

The ability to distinguish individual pores allows the investigation of fluid concentration at the pore level. In Fig. 4(a) we summarize statistics (in the form of box plots [7]) on the distribution of saturations found in pores of different volume ranges. Generally the distributions are skewed, with mean saturation below the 50% quartile at residual fluid conditions. At residual water conditions, it is generally expected that the water (wetting

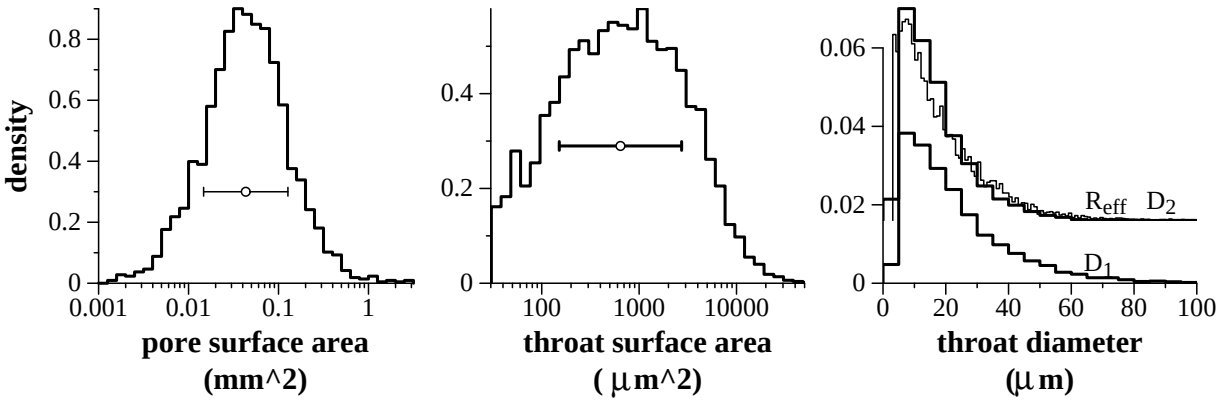

Figure 3. (left) Pore surface area, (middle) throat surface area and (right) throat diameter distributions determined from s_w. (left, middle) The open circle and horizontal bar indicate mean and standard deviation of the distribution. (right) All plots are to the same vertical scale, but D_1 and D_2, have been vertically displaced from each other for visual clarity. R_{eff} (light curve) is drawn with the same vertical displacement as D_2 to emphasize the similarity between the two plots.

Table 1
Comparison of residual saturation values

	image analysis		bulk measurement	
	s_w	s_o	s_w	s_o
s_{wr}	20%		26-29%	
s_{or}		18%		28-32%
gel		35%		31-34%
$gels_{wr}$	32%			
$gels_{or}$		48%		48-50%

Table 2
Water saturation in selected regions

	R_b (8%PV)	R_o (65%PV)
s_{wr}	50%	6%
$gels_{wr}$	100%	0%
s_{or}	96%	76%
gel	92%	53%
$gels_{or}$	80%	38%

phase) saturation should remain close to one (oil saturation close to zero) in the smaller pores. This is not consistent with our data. Calculation using the Young-Laplace equation however, confirms that oil should be able to enter the smallest pores visible with our voxel resolution. Specifically, to enter throats of diameter $\sim 5\mu$m, a capillary pressure around 1 psi is needed. Thus the 17 psi pressure gradient used is sufficiently strong to mobilize water from the smallest pores detectable with our voxel resolution.

Comparison of the s_{or} and gel plots indicates a surprising increase in oil concentration over most pore sizes in spite of the fact that only aqueous gel has been injected. What we are seeing is the appearance of residual oil mobilized by the gel from upstream of the imaged region. Such mobilization has been observed previously [21] and is believed to be produced by the injection of the non-Newtonian fluid (gel).

The effects of the gel on residual fluid distributions can be seen by comparing the s_{wr} distribution with that of $gels_{wr}$ and s_{or} with that of $gels_{or}$. From this comparison it would appear that gelation effects are not correlated strongly with any specific pore size range. Fig. 4(b) summarizes saturation statistics only in throat regions. (Specifically a throat

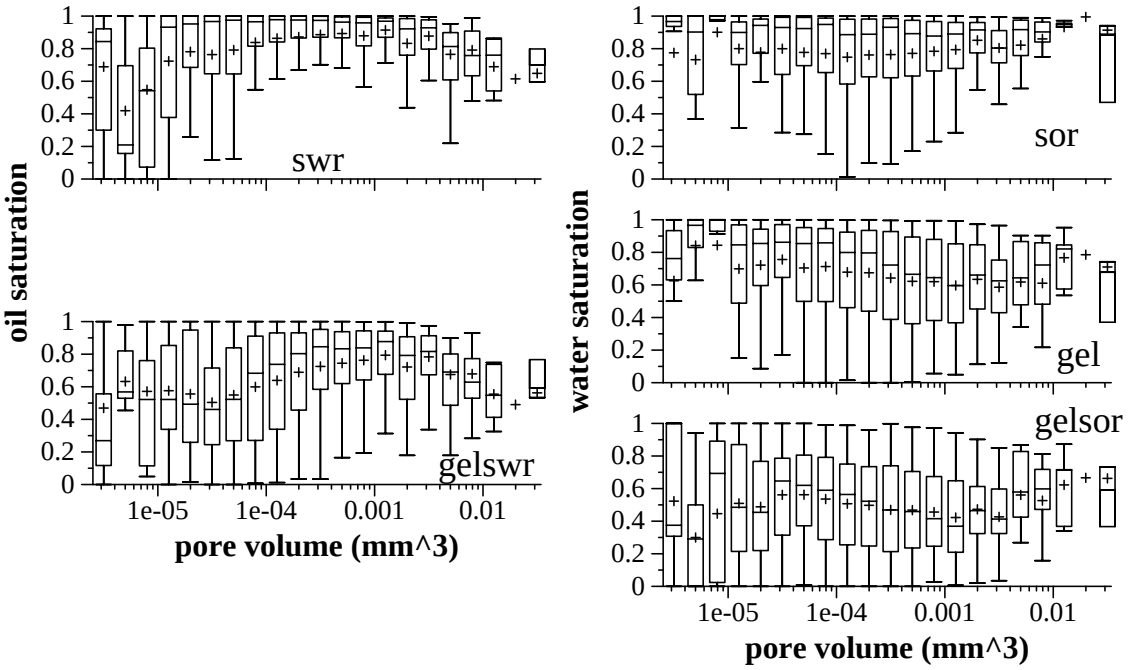

(a)

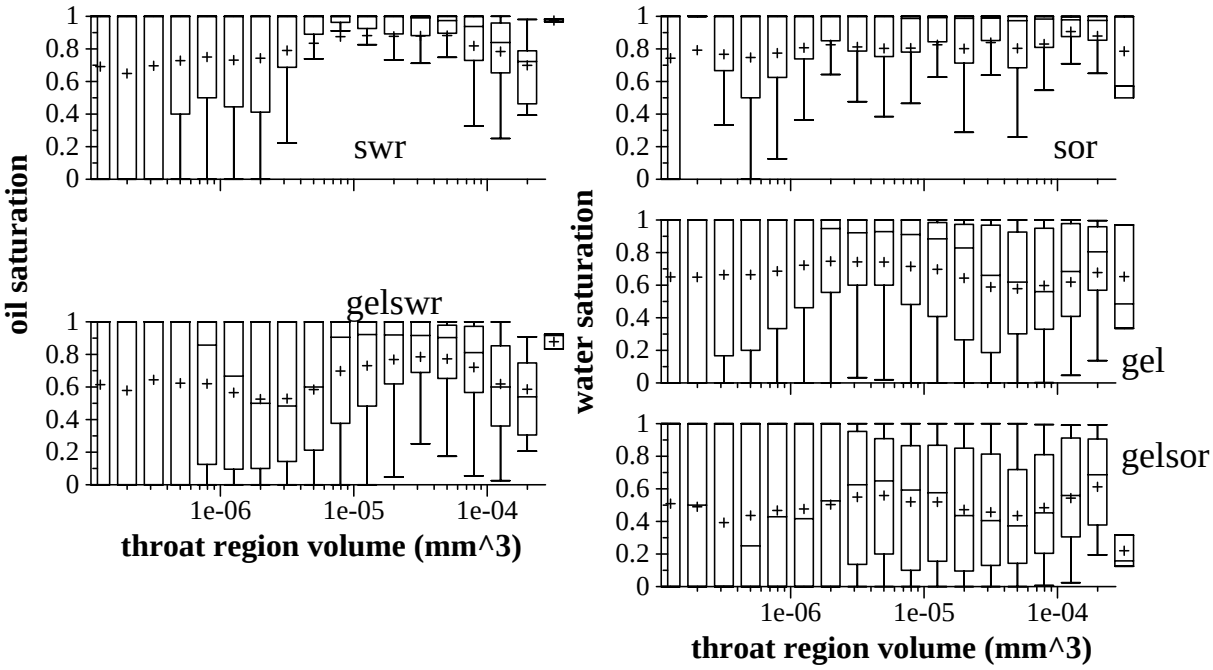

(b)

Figure 4. Distributions of oil saturation (at residual water conditions) and water saturation (at residual oil conditions) as a function of volume for (a) pores and (b) throat regions at the residual fluid conditions investigated. For each volume range, we present a box plot summarizing the distribution of saturations measured in all regions having volume in the specified range.

region is defined as the set of voxels through which a triangulated throat surface passes.) The plots show no significant difference in behavior in fluid fractionation in throat regions compared to pores, indicating that gelation effects are not correlated strongly with any specific throat size range. This eliminates gel blocking at throats as a mechanism for disproportionate permeability reduction.

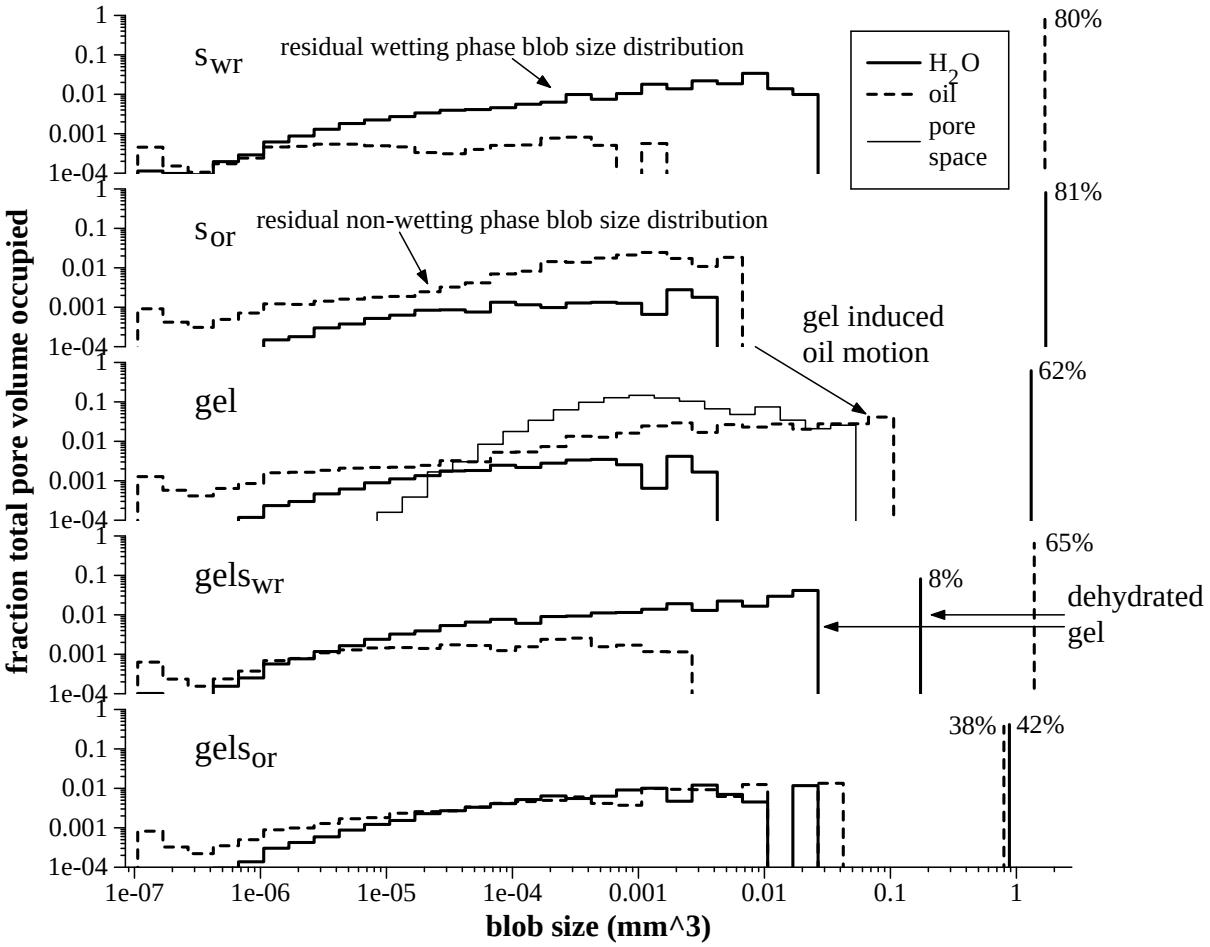

Figure 5. Distribution of water and oil blob sizes in the images s_{wr} through $gels_{or}$. Blob size (x-axis) is given as a volume. The y-axis displays the total volume (expressed as a fraction of the pore volume) occupied by all blobs in each specified size range.

To further investigate gelation effects, we consider the connectivity of the oil and aqueous phases. Treating the wetting phase (brine) as 26-connected and the non-wetting (oil) as 6-connected, we locate the disconnected "blobs" of each fluid phase. The distribution of blob sizes (expressed as volume) determined for each fluid phase, at each residual fluid condition is presented in Fig. 5.

At s_{wr}, there is a continuum of small brine blob (wetting phase) sizes, the largest of which are less than 0.02 mm^3. The non-wetting phase consists of a single large connected oil blob of volume 1.7 mm^3, and a continuum of small oil blobs of size less than 0.002 mm^3. A similar characterization holds for the fluid distributions in the other 4 images. While it makes sense to refer to the actual volumes of those blobs comprising the continuum

spectrum (as these sizes should be determined by the pore size of the rock), the volume of the dominant fluid blob(s) will simply scale with rock volume. We have therefore also displayed the percentage of pore volume occupied by the largest fluid blobs. (These percentages can also be read from the y-axis, though the log-scale makes it difficult.)

In examining Figs. 4 and 5, we caution that conclusions should not be formed on the behavior of the lowest end of the distribution (below $1.2 \cdot 10^{-6}$ mm^3, which corresponds to objects of size 10 voxels or less) since misidentification errors between rock and oil voxels would significantly impact results in this region.

As stated, the continuous part of the blob size distribution should be governed by pore size. To demonstrate this, we replot the pore volume distribution from Fig. 2, now reporting the total volume occupied by all pores in each size range. To keep Fig. 5 uncluttered, we plot this pore volume distribution only on the middle (gel) plot. With one exception, the continuum part of the blob size distributions at each residual fluid condition is, in fact, limited by the size of the largest pore. The exception is the continuum spectrum of oil blobs in gel produced, as mentioned above, by mobilization of upstream residual oil due to the introduction of the non-Newtonian gel. During mobilization there is apparently sufficient merging of oil blobs to result in blobs exceeding the size of the largest pores.

In the transition from gel to gels$_{wr}$, oil saturation increased from 35% to 68% (Table 1). As mentioned, the mechanism for this oil displacement and subsequent restoration of an important level of permeability to oil, is germaine to field applications. Possibilities for the reduction of gel volume include oil i) inducing large amounts of mechanical breakage ("ripping") in the linked polymer network; ii) concentrating (hydrating) the gel - essentially compressing the polymer network; iii) mobilizing the gel; and iv) chemically destroying the gel. As hexadecane is not reactive with any of the gel, brine or rock components, chemical destruction is unlikely. Pressure gradients were closely monitored during floods, and were maintained well below gradients needed to mobilize the gel. In similar, bulk core flood experiments, gel production has never been observed from the core. Our results support the dehydration mechanism. Ripping should occur with predominance in large pores, implying oil saturation increases should be greater in large pores. From Fig. 4(a), oil saturation changes from gel to gels$_{wr}$ appear relatively insensitive to pore size. In fact, with a fixed driving pressure gradient, one would expect gel in all pores to be compressed (hydrated) to the same extent.

Effects of gelation are most strongly evident in comparing gels$_{wr}$ with s$_{wr}$. In gels$_{wr}$ the large residual water blob of volume 0.17 mm^3 (8% PV) and the upper end (above 0.01 mm^3) of the continuum spectrum of water blobs are, we conclude, relatively stationary dehydrated gel blobs. Below 0.01 mm^3, the water blob spectrum of gels$_{wr}$ and s$_{wr}$ are virtually identical, implying these water blobs have been immobile throughout all fluid flushes and may not have been displaced, even by the gel.

Upon further brine injection (gels$_{or}$, Fig. 5), we conjecture the gel does not rehydrate significantly and the pore space is occupied by regions of gel, brine and oil. Some flow paths appear blocked so that a significantly greater fraction of oil becomes trapped. This supports a conjecture that local gel concentration (dehydration) is acting as a blocking mechanism.

To further understand gel behavior, we compare water penetration into two disjoint regions of the pore space. The first region, R_b, occupying 8% PV, is the region occupied

by the largest gel blob at gels_{wr} (Fig. 5). The second region, R_{o}, occupying 65% of the pore volume, is the region occupied by the large oil blob at gels_{wr} (Fig. 5). The percentage volume of each region occupied by water after each stage of flooding is shown in Table 2. From the s_{wr} entry in column 1, we see that R_{b} is a region of natural high residual water. After gel placement, the residual water (gels_{wr} entry, column 1) content of R_{b} is doubled. At s_{or} conditions, of course, the water content in R_{b} is very high, though water injection post gel (gels_{or} entry, column 1) reduces the water content in R_{b} by 20%, indicating that some upstream oil does manage to invade some of this gel space.

In contrast, R_{o} is a region of high oil pentration (entry s_{wr} in column 2) that retains high oil occupancy after gel injection (entry gels_{wr}, column 2). From the corresponding entries for s_{or}, gel and gels_{or}, we see that this high oil occupancy is due to a gel enhanced residual oil component that grows from 24% at s_{or} to 62% at gels_{or}, indicative of oil trapping.

Table 3
Specific surface areas for pore space and dominant blobs

		s_{wr}	s_{or}	gel	gels_{wr}	gels_{or}	
	pore space	oil	brine	brine	oil	brine	oil
σ_f (μm^{-1})		0.0165	0.0120	0.0260	0.0253	0.0366	0.0399
σ_r (μm^{-1})	0.0793	0.0802	0.0710	0.0685	0.0754	0.0587	0.0797

One effect of gel placement is to increase the fluid-fluid surface area for blobs. For a single fluid blob, let a_f denote the area of the blob surface that is in contact with the other fluid phase, and a_r denote the area of the blob surface in contact with rock. Let v_b denote the volume of the blob. Let $\sigma_f \equiv a_f/v_b$ denote the blob's specific fluid surface area and $\sigma_r \equiv a_r/v_b$ denote the blob's specific rock surface area. Table 3 presents the specific surface areas computed for the dominant fluid blobs at each residual condition. At gels_{or}, σ_f for the dominant brine blob has increased by a factor of 3 (compared to s_{or}), while σ_f for the dominant (trapped) oil blob has increased by a factor of 2.5 (compared to s_{wr}). Interestingly, σ_r for the dominant oil blob remains approximately constant before and after gel addition (and in good agreement with σ_v, the rock-void specific surface area (first entry, row 2)), whereas σ_r for the dominant brine blob is always less than σ_v and decreases with gel injection.

In a study on the structure of residual oil saturation, Chatzis et al. [3] reference earlier work [16] on flow in unconsolidated bead packings that found 65% of the oil blobs at residual oil saturation were singlets (i.e. fully contained in single pores), 20% of the blobs were doublets (i.e. spanned two pores), and the rest displayed greater pore occupancy. On the left of Fig. 6 we plot the observed fraction of oil blobs having various pore occupancy numbers for the images s_{or}, gel and gels_{or}. In order to reduce influence of segmentation errors, we ignore all blobs of size smaller than $1.2 \cdot 10^{-5}$ mm^3 in producing this plot. The distributions have similar structure, except for a systematic increase in fraction of blobs with large occupancy numbers in gel resulting from upstream oil blob mobilization and merging upon gel injection. We obtain a singlet frequency of 60% and a doublet frequency of 25%. The number frequency distribution however is quite susceptible to changing the

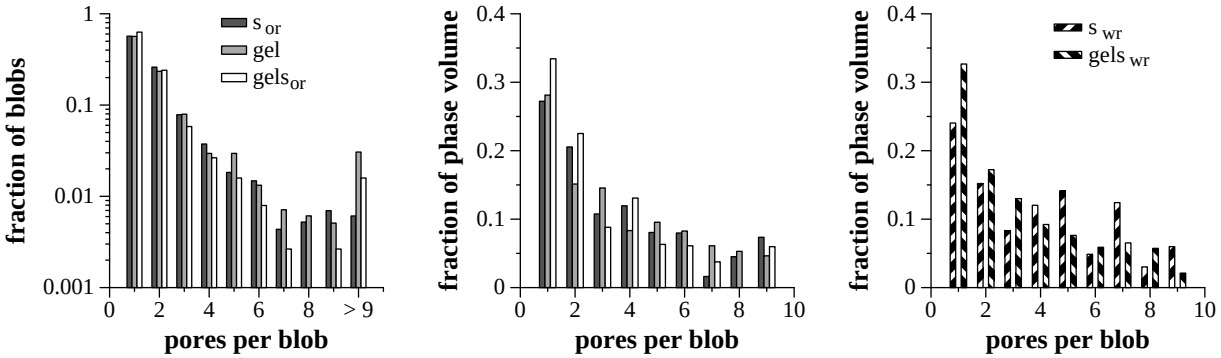

Figure 6. Distribution of blob occupancy

imposed cut-off defining small blob size. To remove this dependence, we consider not the fraction of blobs, but the fractional volume of blobs. Consider **all** blobs having occupancy number **only** in the range $1 \rightarrow 9$. Let V_{1-9} denote the total volume occupied by these blobs. Let $V_{1-9}(i)$ denote the total volume occupied by blobs of occupancy $i, i \in [1, 9]$. The middle plot in Fig. 6 recasts the occupancy distribution in terms of fractional phase volume $f_V(i) \equiv V_{1-9}(i)/V_{1-9}$. By using fractional volume, and ignoring high occupancy (large volume blobs) we reduce the dependency of the distribution on both segmentation errors and on the presence of any very large oil blobs (as appear in gels_{or}) that are not present when gel is absent (s_{or}). Least square fits to a model

$$f_V(i) = f_V(1)\ i^{-\alpha}, \qquad i = 1, \ldots, 9$$

gives consistent values for α of: 0.92 ± 0.26 (s_{or}); 0.78 ± 0.07 (gel); and 0.95 ± 0.16 (gels_{or}), and a value of $f_V(1) = 0.31 \pm 0.03$. The quoted errors for α are 1-standard deviation. The right plot in Fig. 6 provides comparison to the aqueous phase at residual water conditions, s_{wr} and gels_{wr}. The distribution of brine blob occupancy at s_{wr} is quite different from the oil case, as is to be expected since brine is the wetting phase, whereas the distribution at gels_{wr} is similar to the oil case. We interpret this to be a reflection of the presence of the polymeric gel which is the overwhelming residual aqueous component at gels_{wr}.

REFERENCES

1. F.M. Auzerais, J. Dunsmuir, B.B. Ferreol, N. Martys, J. Olson, T.S. Ramakrishnan, D.H. Rothman and L.M. Schwartz, Transport in sandstone: A study based on three dimensional microtomography. Geophys. Res. Lett. 23 (1996) 705.
2. J. Bloomenthal, Polygonization of implicit surfaces. IEEE Comput. Graph. App. 5 (1988) 341.
3. I. Chatzis, N.R. Morrow and H.T. Lim, Magnitude and detailed structure of residual oil saturation. SPEJ 23 (1983) 311.
4. E. Dalla, M. Hilpert and C.T. Miller, Computation of the interfacial area for multi-fluid porous medium systems. J. Contam. Hydro. 56 (2002) 25.
5. H.W. Deckman, J.H. Dunsmuir, K.L. D'Amico, S.R. Ferguson, and B.P. Flannery, Development of quantitative X-ray microtomography, Mater. Res. Soc. Symp. Proc. 217 (1991) 97.

6. B.P. Flannery, H.W. Deckman, W.G. Roberge and K.L. D'Amico, Three-dimensional X-ray microtomography. Science 237 (1987) 1439.
7. HyperStat Online Textbook, http://davidmlane.com/hyperstat/
8. W.B. Lindquist, S.M. Lee, D. Coker, K. Jones and P. Spanne, Medial axis analysis of void structure in three-dimensional tomographic images of porous media. J. Geophys. Res. 101B (1996) 8297.
9. W.B. Lindquist and A. Venkatarangan, Investigating 3D geometry of porous media from high resolution images. Phys. Chem. Earth (A) 25 (1999) 593.
10. W.B. Lindquist, A. Venkatarangan, J. Dunsmuir and T.-f. Wong, Pore and throat size distributions measured from sychrotron X-ray tomographic images of Fontainebleau sandstones. J. Geophys. Res. 105B (2000) 21508.
11. W.B. Lindquist, Network flow model studies and 3D pore structure. Contemp. Math. 295 (2002) 355.
12. W.B. Lindquist, Quantitative analysis of three dimensional X-ray tomographic images. In Developments in X-ray Tomography III, U. Bonse (ed.), Proceedings of SPIE **4503**, 103. SPIE, Bellingham, WA, 2002.
13. W.E. Lorensen and H.E. Cline, Marching cubes: a high resolution 3-D surface construction. ACM Comput. Graph. 21 (1987) 163.
14. M. McKellar and N.C. Wardlaw, A method of making two-dimensional glass micromodels of pore systems. J. Cdn. Pet. Tech. 21 (1982) 39.
15. W. Oh and W.B. Lindquist, Image thresholding by indicator kriging. IEEE Trans. Pattern Anal. Mach. Intell. 21, (1999) 590.
16. R.L. Robinson and R.E. Haring, Experimental study of residual oil configuration in unconsolidated sand. Jersey Prod. Res. Co. Report, Prod. Div. (Jan 1962).
17. R.S. Seright, J.-T. Liang, and H. Sun, Gel treatments in production wells with water coning problems. In Situ 17 (1993) 243.
18. R.S. Seright, J.-T. Liang, W.B. Lindquist, and J.H. Dunsmuir, Characterizing disproportionate permeability reduction using synchrotron X-ray computed microtomography. SPE Reserv. Eval. Eng. 5 (2002) 355.
19. R.S. Seright, J. Liang, W.B. Lindquist and J.H. Dunsmuir, Use of X-ray computed microtomography to understand why gels reduce permeability to water more than to oil. J. Petroleum Sci. Eng. 39 (2003) 217.
20. P. Spanne, J.F. Thovert, C.J. Jacquin, W.B. Lindquist, K.W. Jones and P.M. Adler, Synchrotron computed microtomography of porous media: topology and transports. Phys. Rev. Lett. 73 (1994) 2001.
21. D. Wang, X. Huifen, L. Zhongchun, and Y. Qingyan, Study of the mechanism of polymer solution with visco-elastic behavior increasing microscopic oil displacement efficiency and the forming of steady "oil thread" flow channels. SPE paper #68723 presented at the 2001 SPE Asia Pacific Oil and Gas Conference and Exhibition, Jakarta, Indonesia, Apr. 17-19, 2001.
22. D. Wildenschild, J.W. Hopmans, C.M.P. Vaz, M.L. Rivers, D. Rikard and B.S.B. Christensen, Using X-ray computed tomography in hydrology: systems, resolutions, and limitations. J. Hydro. 267 (2002) 285.